On the Variability of Mesospheric OH Emission Profiles

Romina Nikoukar
University of Illinois at Urbana-Champaign

Gary R. Swenson
University of Illinois at Urbana-Champaign

Alan Z. Liu
Embry Riddle Aeronautical University - Daytona Beach, liuz2@erau.edu

Farzad Kamalabadi
University of Illinois at Urbana-Champaign

On the variability of mesospheric OH emission profiles

Romina Nikoukar,[1] Gary R. Swenson,[1] Alan Z. Liu,[1] and Farzad Kamalabadi[1]

[1] Mesospheric OH radiance limb profiles measured by the Sounding of the Atmosphere using Broadband Emission Radiometry (SABER) instrument aboard the Thermosphere Ionosphere Mesosphere Energetics and Dynamics (TIMED) spacecraft were inverted to yield altitude profiles of OH volume emission rates. The Abel inversion results of two months of data (from 1 June to 31 July 2004) were analyzed for the layer mean and standard deviation as a function of latitude and local time. Statistical analysis of SABER data shows that the global difference between the mean and standard deviation profiles for the OH(v_u = 7, 8, 9; Δv = 2) emission (at 2.0 μm) is approximately 2.8 km, very similar to the theoretical model prediction by Liu and Swenson (2003). This agreement is an indication that these variations from the mean are likely caused by atmospheric tides and gravity waves.

Citation: Nikoukar, R., G. R. Swenson, A. Z. Liu, and F. Kamalabadi (2007), On the variability of mesospheric OH emission profiles, *J. Geophys. Res.*, *112*, D19109, doi:10.1029/2007JD008601.

1. Introduction

[2] Mesospheric airglow layers in the 80–100 km altitude range have been the subject of extensive investigation to provide dynamic and temperature information using remote sensing spectrometers, imagers, and interferometers. These layers have been recognized as containing brightness and temperature variations attributed to the passage of atmospheric waves through the layers. The phase information of perturbed brightness, for example, provides information about the vertical wavelength of waves if the separation between the layers is well known [*Liu and Swenson*, 2003].

[3] Observations of wave structure in the hydroxyl airglow layer have been performed from the ground and space by a number of investigators, e.g., *Krassovsky* [1972], *Krassovsky and Shagaev* [1974], *Hecht et al.* [1995], *Lowe and Turnbull* [1995], *Reisin and Scheer* [1996], *Oznovich et al.* [1997], *Shiokawa et al.* [2003], and *López-González et al.* [2004, 2005]. These observations include oscillations with periods across the spectrum of planetary waves, tides, and atmospheric gravity waves. The photochemical processes and rate coefficients have been a source of investigation, and from a standpoint of current definition, we recognize the work of *McDade et al.* [1987] for the hydroxyl emission chemistry.

[4] Hydroxyl airglow responses to atmospheric gravity waves (AGWs) have been modeled extensively [e.g. *Walterscheid et al.*, 1987; *Hickey*, 1988a, 1988b; *Tarasick and Shepherd*, 1992; *Swenson and Gardner*, 1998; *Liu and Swenson*, 2003; *Vargas et al.*, 2007]. We note that the intrinsic nature of atmospheric perturbations due to AGWs and tides are the same in the mesosphere, and consequently modeled responses generally apply to both processes. *Swenson and Gardner* [1998] modeled the OH layer response to a high frequency gravity wave, where they found that the wave–induced variability of the emission intensity altitude profile was much larger on the bottom side of the layer than the top side. In fact, the peak of emission perturbation was modeled to be 3.75 km below the emission peak altitude, while the peak of rotational temperature was modeled to be near the peak of the emission layer. *Liu and Swenson* [2003] refined the model in terms of the background atomic oxygen density profile, and deduced a difference of 3.1 km. This separation between the peaks of the emission layer and the layer perturbations is the major explanation for the phase difference between OH brightness and rotational temperature perturbations observed in the airglow studies, and is indicative of the wave's vertical wavelength.

[5] Although the airglow responses to atmospheric gravity waves have been modeled theoretically, to date few empirical studies have been conducted to validate these models. As an example, we mention the work of *Lowe et al.* [1996] where they present six average profiles of OH volume emission rate (VER) along with corresponding standard deviation (Std.) profiles taken on 1 March 1993 by WINDII/UARS with the altitude separation between the peaks of the average and perturbed profiles evident in their results. Their analysis, however, was limited to the equinox midlatitudes at local times from 2300 to 0145 h.

[6] The motivation for this study is to present experimental evidence of the modeled altitude differences between the OH volume emission layer peak and the maximum of the wave-induced variability of the layer for a wide range of latitudes. In this paper, we examine the statistics of the hydroxyl VER altitude profiles in terms of mean and standard deviation of the layer, as observed by the Sounding of the Atmosphere using Broadband Emission Radiom-

[1]Department of Electrical and Computer Engineering, University of Illinois at Urbana-Champaign, Coordinated Science Laboratory, Urbana, Illinois, USA.
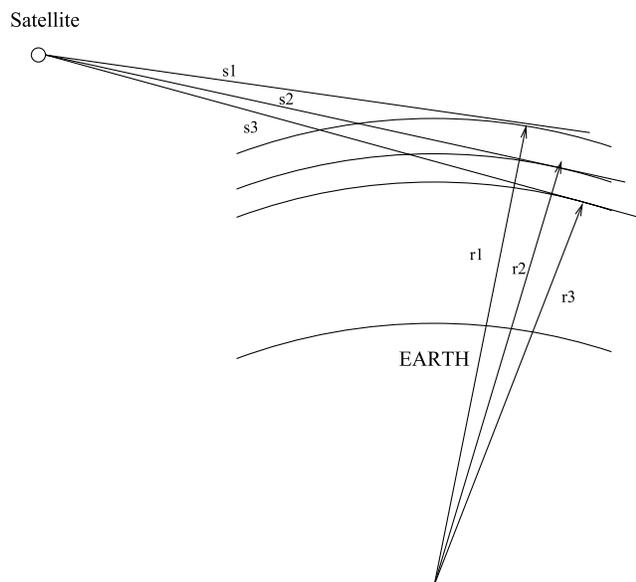
Satellite

Figure 1. Line-of-sight measurements (s_1, s_2 and s_3) along with several altitude shells (r_1, r_2 and r_3) used in a typical Abel inversion.

etry (SABER) instrument aboard the Thermosphere Ionosphere Mesosphere Energetics and Dynamics (TIMED) satellite. The measurements are then compared to the predicted differences modeled by *Liu and Swenson* [2003] and *Swenson and Gardner* [1998]. Upon agreement with the theoretical models, these results would provide a basis for understanding the phase separation for waves propagating through the layers.

2. Construction of OH Volume Emission Rate

2.1. Observations

[7] The SABER instrument is one of four instruments onboard the TIMED satellite. SABER is a 10-channel Earth-limb-scanning radiometer designed to measure key infrared atmospheric emissions in the 1.27 μm to 15 μm spectral range including carbon dioxide, ozone, nitric oxide, water vapor and excited states of molecular oxygen and hydroxyl [*Mlynczak*, 1997; *Russell et al.*, 1999]. The fields of view (FOV) of SABER's 10 detectors are scanned across the Earth limb by means of a one-axis scan mirror to produce radiance profiles of the above-mentioned emissions. The limb profiles are presented as a function of tangent height, which is the altitude of the point of closest approach of an emission raypath to the Earth surface. Measurements over the tangent altitude range from 400 km to below the Earth surface are repeated at intervals of approximately 64 s, corresponding to a motion along the satellite track of about 480 km. The instrument field of view full width at half maximum (FWHM) for all channels meets specifications of 0.7 mrad or 2 km at the tangent height point for the 625 km nominal orbit altitude.

[8] Two of the 10 radiometers on the SABER instrument measure the limb profiles of the OH(v_u = 7, 8, 9; Δv = 2) and (v_u = 4, 5, 6; Δv = 2) Meinel bands at 2.0 μm and 1.6 μm, respectively. In this paper, we focus on the analysis of

SABER 2.0 μm OH observations since these high vibrational bands, v = 7, 8 and 9, are common to those modeled by *Swenson and Gardner* [1998] and *Liu and Swenson* [2003]. The level 1B data, available at http://saber.larc.nasa.gov, contains the preprocessed OH emission radiance profiles, where the volumetric contribution of the FOV is converted to a line integral through deconvolution methods. With this conversion, we may represent the limb profiles as a series of line of sight measurements of VER:

$$I_i = \int_{-\infty}^{\infty} V(s_i)ds_i \quad \text{for } i = 1, 2, \dots, \tag{1}$$

where I_i is the ith emission radiance measured along the slant direction s_i, and $V(s_i)$ and ds_i represent the OH volume emission rate and incremental distance along this slant direction, respectively (see Figure 1).

2.2. Analysis Technique

[9] The goal of the inversion is to recover the unknown VER from its line integrals. In this work, we perform the inversion using the Abel technique [*Zwillinger*, 1996], where it is assumed that the observed emission does not vary along the satellite track but with altitude only (see Figure 1).

[10] The unknown VER can be obtained using the expression for the inverse Abel transform:

$$V(r) = -\frac{1}{\pi} \int_r^{\infty} \frac{\frac{d}{dp}I(p)dp}{(p^2 - r^2)^{1/2}}, \tag{2}$$

where $V(r)$ represents the volume emission rate at radius r (from the center of the Earth) as a function of emission radiance (I) at larger radii (p). Therefore the recovered function (in the Abel inversion) at radius r depends only on the values of line integrals at radii greater than r. Although the Abel inversion suffers from the simplified assumption of spherical symmetry, this method implies no systematic distortion of the desired profiles and is appropriate for limb scanning observations [*Solomon et al.*, 1984]. Moreover, the Abel inversion is more straightforward to implement than other types of inversion. In this work, we present the statistical analysis of the Abel inverted OH radiance profiles measured by the SABER instrument.

3. Statistical Analysis Results

[11] Through statistical analysis, we attempt to verify the theoretical models of the effect of gravity waves on the hydroxyl VER using satellite data for the first time. For this purpose, we examine the Abel inverted radiance profiles measured by SABER from 1 June to 31 July 2004 (days 153 to 213). During the first half of this 2-month period, the instrument was oriented to look toward the north pole providing a latitude coverage from 50°S to 80°N. The latitude range from 50°N to 80°S was covered during the second half of this period. The inverted radiance profiles (or equivalently VER profiles) are binned with respect to local time and latitude. We choose the local time bins as follows: evening (1700–1900 h), early night (2000–2200 h), late night (2300–0100 h) and early morning (0200–0400 h).
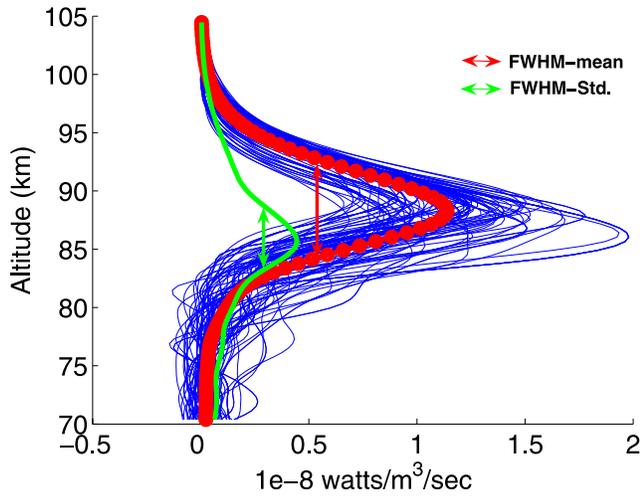
Figure 2. OH 2.0 μm inverted profiles from 0200 to 0400 h for northern midlatitudes along with the mean and standard deviation of the layer. Thin blue curves represent the retrieved OH VER profiles whereas the red and green curves illustrate the mean emission layer and the standard deviation of the layer with respect to the mean. The red and green arrows illustrate the FWHM of the mean and Std. layers, respectively.

The latitude bins include the low latitudes (between $0°$ and $30°$), mid latitudes (between $30°$ and $60°$) and high latitudes (between $60°$ and $80°$). This classification of the latitude regions is based on the knowledge that diurnal atmospheric tides affect mostly the low latitude regions and hence the statistical analysis would reveal local time effects of tides on the OH layer at these regions (such as observed by *Zhao et al.* [2005]).

[12] The statistical analysis is performed by obtaining the mean and standard deviations of the inverted radiance profiles in each time period and latitude bin. The standard deviation profile represents the perturbation of the VER profiles with respect to the mean layer and can be regarded as a measure of variability of the layer. Figure 2 illustrates an example of various OH VER profiles (in blue) from 0200 to 0400 h for northern midlatitude along with the mean and standard deviation curves (in red and green, respectively). An important feature is that the perturbations are not symmetric with respect to the altitude of the maximum mean emission, and in fact, the deviations from the mean are stronger at altitudes below the mean layer peak. The centroid height of the standard deviation profile is at 85.6 km, which is 2.7 km lower than the centroid height of the mean layer (Table 1). Another interesting observation is the decrease of the peak altitude with increasing volume emission rate. A similar property has been pointed out in the work by *Liu and Shepherd* [2006], where they use WINDII/UARS observations.

[13] Figures 3–8 represent the mean and standard deviation profiles obtained by a similar analysis performed on the data from different time periods and different latitude ranges. By inspecting these figures, we can make the following observations:

[14] 1. As in Figure 2, all these figures share the common property that the profiles exhibit peak Std. heights which are lower than the layer mean maximum altitudes indicating more variability in the extracted VER in the lower altitudes regardless of the latitude or time.

[15] 2. The average of the difference between centroid heights of all retrieved mean and standard deviation profiles can be estimated as 2.8 km ± 0.7 km. In addition, the FWHM of the mean layer is larger than that of the standard deviation layer by about 3.7 km ± 1.2 km. Table 1 along with the plots in Figures 9a–9f summarize all the information regarding the centroid height of the mean layer and its standard deviation as well as the FWHM of each layer corresponding to the four time periods and the three latitude regions in the northern and southern hemispheres. Table 2

Table 1. Summary of Peak Height (km) and FWHM (km) of the OH 2.0 μm Mean and Std. Layers for Different Latitude Ranges and Time Period[a]

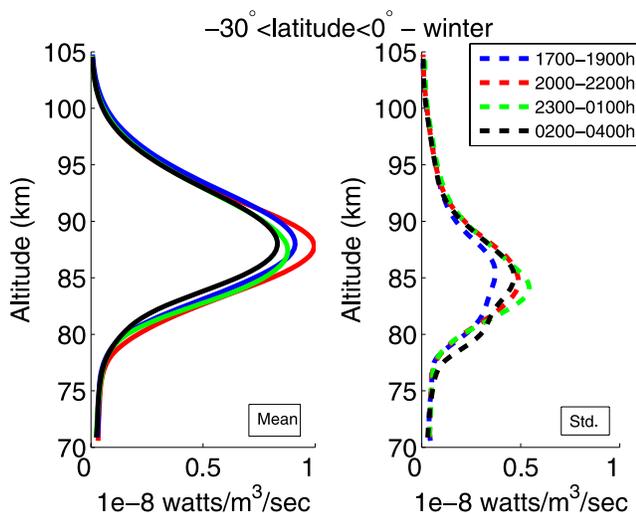|	1700–1900h		2000–2200h		2300–0100h		0200–0400h	
	Peak, km	FWHM, km	Peak	FWHM	Peak	FWHM	Peak	FWHM
$0° \leq$ Latitude $\leq 30°$-summer	[2143]		[4809]		[12,979]		[5469]	
Mean	88.5	10.8	88.8	9.8	87.9	10.8	87.9	10.7
Std.	87.0	7.3	86.4	5.2	85.1	6.7	84.8	6.2
$-30° \leq$ Latitude $\leq 0°$-winter	[4559]		[11,913]		[14,595]		[4804]	
Mean	87.8	10.5	88.2	11.1	87.8	11.2	88.2	10.6
Std.	84.8	7.6	85.0	6.5	85.1	5.6	84.6	7.2
$30° \leq$ Latitude $\leq 60°$-summer	[495]		[1999]		[6877]		[12,066]	
Mean	88.0	9.4	88.4	9.2	88.7	8.2	88.3	8.1
Std.	85.8	8.8	85.4	5.6	85.7	5.4	85.6	4.9
$-60° \leq$ Latitude $\leq -30°$-winter	[5868]		[14,987]		[15,848]		[4937]	
Mean	86.4	8.8	87.3	10.5	87.5	10.0	86.7	10.6
Std.	83.6	6.6	83.9	6.5	84.3	5.6	83.1	5.9
$60° \leq$ Latitude $\leq 80°$-summer	[0]		[1777]		[646]		[56]	
Mean	N/A	N/A	87.1	6.8	88.2	8.1	87.0	7.1
Std.	N/A	N/A	86.1	4.8	84.4	4.3	84.8	5.1
$-80° \leq$ Latitude $\leq -60°$-winter	[26]		[9]		[1840]		[0]	
Mean	86.6	9.5	86.3	9.9	86.4	10.3	N/A	N/A
Std.	83.7	5.1	84.9	6.4	83.4	6.19	N/A	N/A

[a]The numbers in square brackets denote the number of available profiles for each bin. N/A denotes the unavailability of data at the corresponding latitude regions and local times.
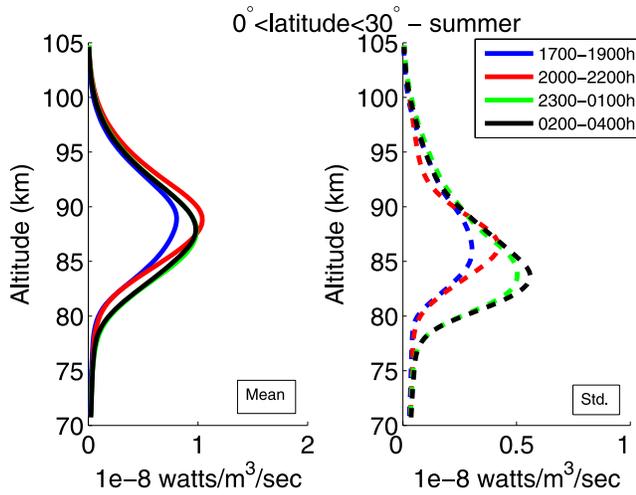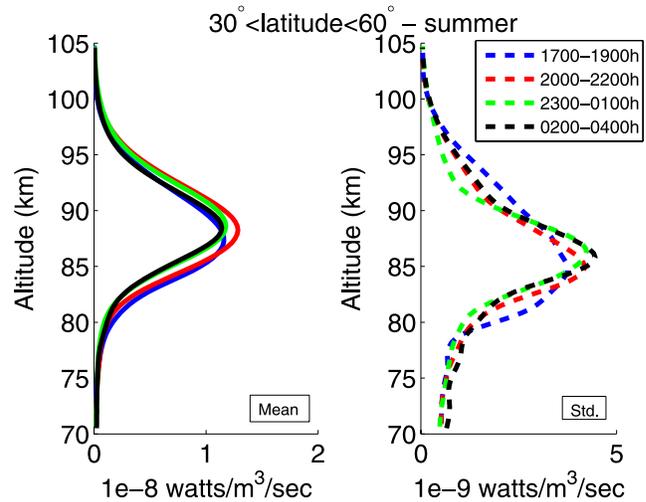
Figure 3. Mean and standard deviation of the OH 2.0 μm volume emission rate for different time periods in the low-latitude regions ($0 < $ latitude $< 30°$) in the northern hemisphere (summer time). The solid lines represent the mean of the VER with respect to altitude (left panel), while the dashed lines represent the standard deviation profiles (right panel).

lists the statistics regarding these four parameters (mean and Std. layers peak altitudes and FWHM) over the night for all latitude regions. Table 3 summarizes the results of a similar statistical analysis performed on the OH 1.6 μm emission. Although the differences between the peaks of the mean and Std. profiles are similar in both cases, the peak altitudes and FWHMs of the mean profiles differ significantly. This difference between the peaks and FWHMs of the two emissions is currently under investigation.

[16] 3. A systematic difference between the peak heights of both mean and Std. layers in northern and southern latitudes is observed. This difference is nearly 1 km and
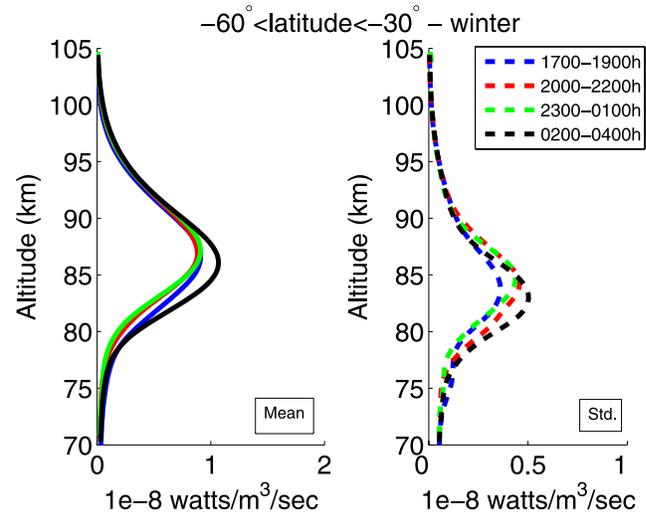

Figure 5. Same as Figure 3 but for midlatitude regions in the northern hemisphere (summer time).

1.2 km for the mean layer and Std. layer, respectively. We believe this difference is primarily due to the upwelling (downwelling) of the atmosphere in the summer (winter) hemisphere, which changes the peak of atomic oxygen profile.

4. Discussion

[17] In their work, *Swenson and Gardner* [1998] described the mechanism responsible for the asymmetry of the perturbation in the lower and upper altitudes for the hydroxyl airglow due to the passage of a gravity wave. They modeled the wave-induced perturbation in the layer as a result of perturbations in atomic oxygen (O), molecular oxygen (O_2) and temperature (T) using the following reactions resulting in the excited OH (equation (3) as a third-body

**Figure 4.** Same as Figure 3 but for low latitudes in the southern hemisphere (winter time).

Figure 6. Same as Figure 3 but for midlatitude regions in the southern hemisphere (winter time).
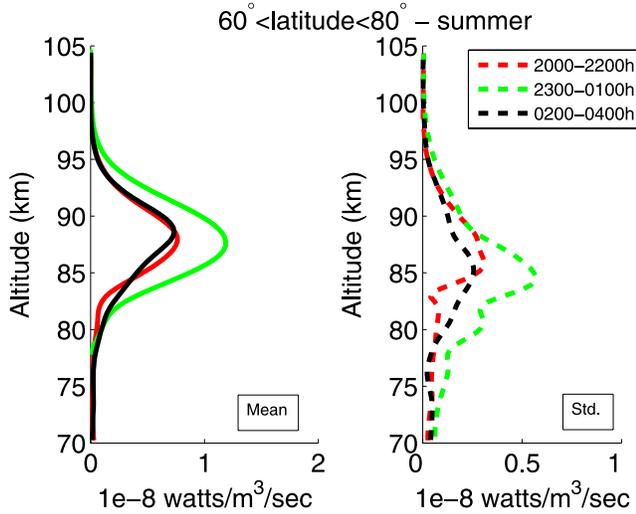
Figure 7. Same as Figure 3 but for high-latitude regions, in the northern hemisphere (summer time).

reaction and equation (4)) and the following expression for the hydroxyl volume emission rate (equation (5)):

$$O + O_2 + M \longrightarrow O_3 + M, \qquad (3)$$

$$H + O_3 \longrightarrow OH^* + O_2, \qquad (4)$$
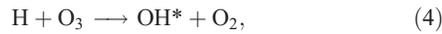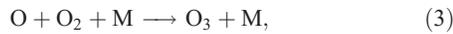
$$V = \frac{K_1[O][O_2](200/T)^{2.5}}{1 + 7.7 \times 10^{-14} cm^3[O_2]}, \qquad (5)$$

where V is the VER of OH(8−3) band and $K_1 = 8.25 \times 10^{-36} cm^6 \ s^{-1}$ is the rate coefficient. The OH* VER perturbations are calculated by differentiating (5) with respect to O, O_2 and T:

$$\Delta V = \frac{\delta V}{\delta[O]}\Delta[O] + \frac{\delta V}{\delta[O_2]}\Delta[O_2] + \frac{\delta V}{\delta[T]}\Delta[T] \qquad (6)$$

where Δ denotes the perturbation. Using a Chapman function approximation for a typical MSIS90 [Hedin, 1991] atomic oxygen profile and MSIS90 molecular oxygen and temperature profiles for midlatitude (40°), Swenson and Gardner [1998] presented analytical expressions for the wave−induced perturbations of the layer, a schematic example of which is illustrated in their Figure 7a. The data plotted in that figure provide considerable insight into the relative contributions of the various parameters to the OH* fluctuations. Herein, we adopt the following explanations for the asymmetry in the layer perturbation across the altitude from their work: the atomic oxygen perturbations (ΔV_O) are very large and 180° out of phase with the atmospheric density perturbations. This feature results from the steep positive gradient with altitude in O in the region of the OH* layer. Due to a shallower negative gradient of the atmospheric density with altitude, the density contribution is smaller. The temperature contribution to ΔV (ΔV_T) is in phase with the atmospheric density contribution but it has

only half the magnitude. When the three individual contributions are summed to give the total volume emission perturbation, ΔV_O is the dominating term. Hence the total OH* fluctuations are largest in the bottomside of the layer where they are dominated by wave induced perturbations in the atomic oxygen profile.

[18] In a separate work, Liu and Swenson [2003] investigated the effect of a single-frequency gravity wave on two airglow layers, OH and O_2 atmospheric band. For their model they obtained the unperturbed temperature, atmospheric density and number densities of various constituents from MSIS90 model at 35°N for spring equinox condition. The wave period and the vertical wavelength of the gravity wave were chosen to be 2 hr and 25 km, respectively. Their results, which were numerically obtained, are in general agreement with those obtained by Swenson and Gardner [1998] in terms of larger variations of the airglow VER in the lower altitudes, although the separation between the predicted maximum OH and the OH mean layer differs in the two papers: 3.1 km in the work of Liu and Swenson [2003] versus 3.75 km obtained by Swenson and Gardner [1998]. This difference is mainly attributed to different modeling methodologies (numerical versus analytical approximations) in addition to differences in the assumed atomic oxygen model profile and input wave parameters. The data plotted in Figure 10, adopted from Liu and Swenson [2003], show typical perturbations of the hydroxyl layer generated by a gravity wave with the mean and Std. layers denoted by the thick solid and thin dashed lines. These perturbations exhibit similar characteristics in terms of maximum variations at lower altitude as the layer perturbations in Figure 2 obtained from SABER limb measurements.

[19] Along with similar results obtained from the 2003 SABER data (not shown here), the results presented in Figures 9a–9f and Table 1 demonstrate that the wave-induced perturbations in the airglow layer show similar behavior in terms of peak height and FWHM, regardless of latitude or local time. This implies that both gravity waves and tides produce larger perturbations in the bottom-
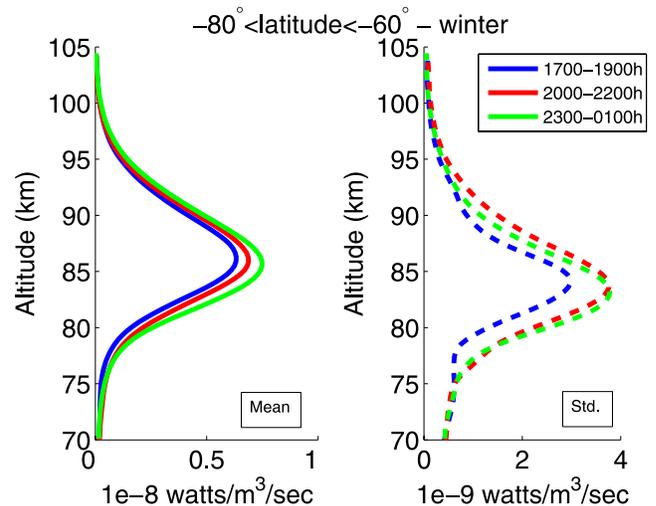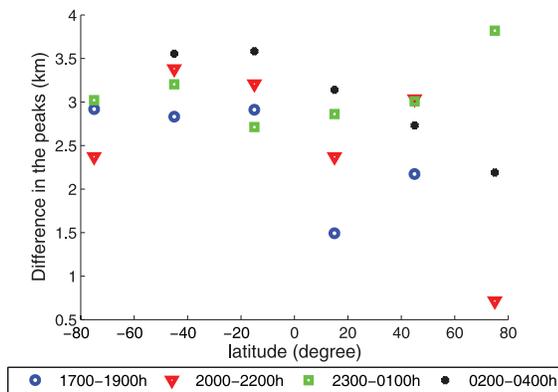

Figure 8. Same as Figure 3 but for high-latitude regions, in the southern hemisphere (winter time).
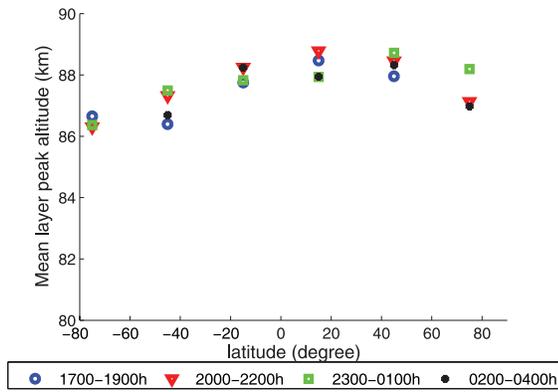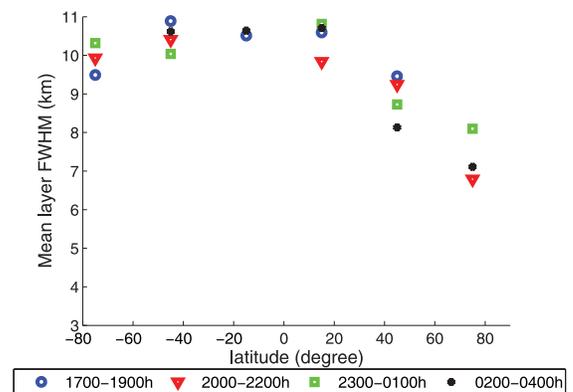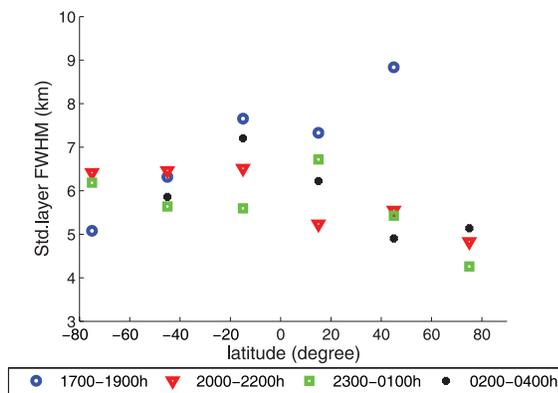
(a) Peak altitude of the mean layer.
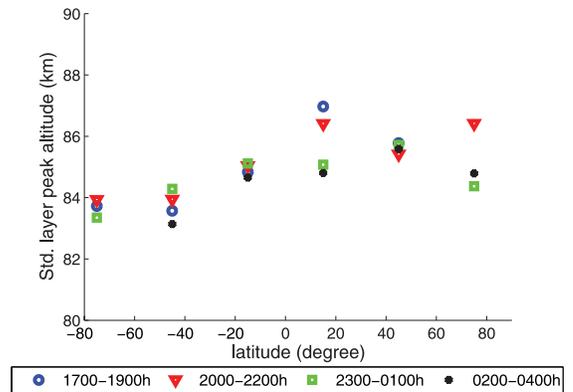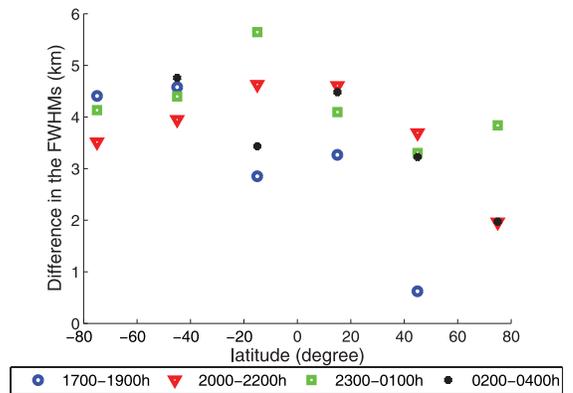
(b) Peak altitude of the Std. layer.

(c) Difference between the peaks of the mean and Std. layers.

(d) FWHM of the mean layer.

(e) FWHM of the Std. layer.

(f) Difference between the FWHMs of the mean and Std. layers.

Figure 9. Distribution of peak altitude and FWHM of the mean and standard deviation layers of the OH 2.0 μm nightglow emission as a function of latitude and local time.

side of the layer, mainly due to variations in the atomic oxygen density.

[20] Although the separation of the peak altitude of the mean and Std. layers is in general agreement with the model predictions by *Swenson and Gardner* [1998] and *Liu and Swenson* [2003], the FWHM of the Std. layers derived from SABER measurements differs from that predicted by the theoretical models. This difference between the modeled and data-driven perturbations has already been recognized in *Swenson and Gardner* [1998], where a modeled per-

Table 2. The Average and Variation of Peak Height (km) and FWHM (km) of the OH 2.0 μm Mean and Std. Layers Over the Course of Night for All Latitude Regions

	Mean Layer	Std. Layer	Difference Between the Mean and Std. Layers
Peak altitude, km	87.6 ± 0.8	84.9 ± 1.0	2.8 ± 0.7
FWHM, km	9.8 ± 1.3	6.1 ± 1.1	3.7 ± 1.2

turbed layer is compared against the hydroxyl measurements from WINDII/UARS in the work by *Lowe et al.* [1996] [see *Swenson and Gardner*, 1998, Figure 7b], and the model perturbation is shown to be thicker by approximately 3 km ($\sim$28%). The same is true for the SABER–derived Std. layers, where this difference is nearly 3.7 km. Since in the simplified one-dimensional chemical models, the wave-induced variations of the layer shape traces directly to the vertical distribution of atomic oxygen, one may argue that this difference in the FWHM of the Std. layer may be due to the lack of a more accurate specification of O profile (especially at the bottomside). While the Chapman layer model provides a reasonable fit to the MSIS90 profile and accurately represents the long-term averaged O profile, it may not be appropriate in all situations. This observation indicates the necessity of improving the existing atmosphere O models to enhance the performance of the theoretical models in characterizing the airglow response to gravity waves.

[21] We need to also point out that our statistical analysis results include both temporal and spatial variabilities of OH VER. Unlike a ground based observation, where most of variabilities can be attributed to passage of gravity waves and tides, satellite observations are not made at a fixed location. Large scale spatial variability, such as from planetary waves, may also contribute to our analysis results. The agreement of the vertical offset between the mean and standard deviation profiles with model, however, suggests that most of the variabilities are due to gravity waves or tides.

5. Conclusion

[22] This paper presents a detailed empirical analysis of the nighttime hydroxyl VER variability as a function of latitude and local time. This study has been conducted to validate the theoretical models that predict the effects of atmospheric gravity waves on the airglow layers. For this purpose, we first recover the hydroxyl VER from the SABER limb profiles by applying the Abel inversion technique. We then estimate the mean and standard devia-

tion of a large set of sample profiles, recovered from 2 months of data. The results of this study are summarized in the following:

[23] 1. The OH 2.0 μm VER profiles from all the bins of interest, show a similar behavior of exhibiting larger variations at heights lower than the mean peak. The average difference between the mean and standard deviation peak heights for all regions and time periods is found to be 2.8 km ± 0.7 km, which is less (10%) than the *Liu and Swenson* [2003] model predictions.

[24] 2. The perturbation of the OH layer, i.e., the deviation of the profiles from the mean, show a smaller FWHM compared to the mean layer in all bins of interest by approximately 3.7 km ($\sim$40%).

[25] 3. Although the differences between the peaks of the mean and Std. profiles are similar for both OH 2.0 μm and OH 1.6 μm emissions, the peak altitudes and FWHMs of the mean profiles differ significantly (see Tables 2 and 3).

[26] 4. Wave-induced perturbations in the airglow layer show similar behavior in terms of peak height and FWHM, regardless of latitude or local time. This implies that both gravity waves and tides produce larger perturbations in the bottomside of the layer, mainly due to variations in the atomic oxygen density.

[27] 5. The SABER-derived standard deviation profiles show lower FWHM than the modeled Std. profiles of about 3.5 km (or 32%). This difference may indicate the lack of a more accurate specification of O profile (especially at the bottomside). Thus in order to enhance the performance of
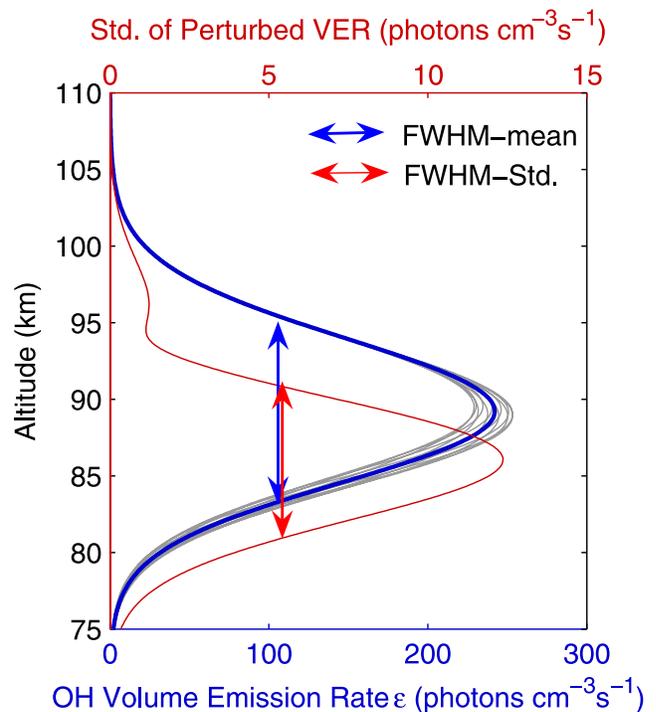
Figure 10. (From *Liu and Swenson* [2003]) Unperturbed (thick solid line) and perturbed (thin dashed gray lines) OH volume emission rate, generated by a gravity wave perturbation. The blue and red arrows represent the FWHM of the mean and Std. layers, respectively.

Table 3. The Average and Variation of Peak Height (km) and FWHM (km) of the OH 1.6 μm Mean and Std. Layers Over the Course of Night for All Latitude Regions

	Mean Layer	Std. Layer	Difference Between the Mean and Std. Layers
Peak altitude, km	85.7 ± 1.1	83.0 ± 1.3	2.7 ± 0.7
FWHM, km	7.7 ± 0.9	6.6 ± 1.0	1 ± 1.3

theoretical models one needs to improve the accuracy of the atmospheric O density models.

[28]   6. Although large scale spatial variability, such as from planetary waves, may also contribute to our statistical analysis results, the agreement of the vertical offset between the mean and standard deviation profiles with model suggests that most of the variabilities are due to gravity waves or tides.

References

Hecht, J. H., S. K. R. Howat, R. L. Walterscheid, and J. R. Isler (1995), Observations of variations in airglow emissions during ALOHA-93, *Geophys. Res. Lett.*, *22*, 2817–2820, doi:10.1029/95GL03019.

Hedin, A. E. (1991), Extension of the MSIS thermosphere model into the middle and lower atmosphere, *J. Geophys. Res.*, *96*(A2), 1159–1172.

Hickey, M. P. (1988a), Effects of eddy viscosity and thermal conduction and Coriolis force in the dynamics of gravity wave driven fluctuations in the OH nightglow, *J. Geophys. Res.*, *93*(A5), 4077–4088, doi:10.1029/88JA01124.

Hickey, M. P. (1988b), Wavelength dependence of eddy dissipation and Coriolis force in the dynamics of gravity wave driven fluctuations in the OH nightglow, *J. Geophys. Res.*, *93*(A5), 4089–4101, doi:10.1029/88JA01125.

Krassovsky, V. I. (1972), Infrasonic variations of the OH emission in the upper atmosphere, *Ann. Geophys.*, *28*, 739–746.

Krassovsky, V. I., and M. V. Shagaev (1974), Inhomogeneities and wavelike variations of the rotational temperature of atmospheric hydroxyl, *Planet. Space Sci.*, *22*, 1334–1337.

Liu, G., and G. G. Shepherd (2006), An empirical model for the altitude of the OH nightglow emission, *Geophys. Res. Lett.*, *33*, L09805, doi:10.1029/2005GL025297.

Liu, A., and G. Swenson (2003), A modeling study of O$_2$ and OH airglow perturbations induced by atmospheric gravity waves, *J. Geophys. Res.*, *108*(D4), 4151, doi:10.1029/2002JD002474.

López-González, M., et al. (2004), Seasonal variations of O$_2$ atmospheric and OH(6-2) airglow and temperature at mid-latitudes from SATI observations, *Ann. Geophys.*, *22*, 819–828.

López-González, M., E. Rodríguez, G. Shepherd, S. Sargoytchev, M. Shepherd, V. Aushev, S. Brown, M. García-Comas, and R. Wiens (2005), Tidal variations of O$_2$ Atmospheric and OH(6-2) airglow and temperature at mid-latitudes from SATI observations, *Ann. Geophys.*, *23*, 3579–3590.

Lowe, R. P., and D. N. Turnbull (1995), Comparison of ALOHA-93, ANLC-93 and ALOHA-90 observations of the hydroxyl rotational tem-perature and gravity wave activity, *Geophys. Res. Lett.*, *22*, 2813–2816, doi:10.1029/95GL02671.

Lowe, R., L. LeBlanc, and K. Gilbert (1996), WINDII/UARS observation of twilight behavior of the hydroxyl airglow, at midlatitude equinox, *J. Atmos. Terr. Phys*, *58*, 1863–1869.

McDade, I. C., E. J. Llewellyn, D. P. Murtagh, and R. G. H. Greer (1987), Eton 5: Simultaneous rocket measurements of the OH meinel? $\Delta v = 2$ sequence and (8, 3) band emission profiles in the nightglow, *Planet. Space Sci.*, *35*, 1137–1147.

Mlynczak, M. (1997), Energetics of the mesosphere and lower thermosphere and the SABER experiment, *Adv. Space Res.*, *20*(6), 1177–1183.

Oznovich, I., R. L. Walterscheid, G. G. Sivjee, and D. J. McEwen (1997), On Krassovsky's ratio for ter-diurnal hydroxyl oscillations in the winter polar mesopause, *Planet. Space Sci.*, *45*, 385–394.

Reisin, E. R., and J. Scheer (1996), Characteristics of atmospheric waves in the tidal period range derived from zenith observations of O$_2$(0-1) atmospheric and OH(6-2) airglow at lower midlatitudes, *J. Geophys. Res.*, *101*, 21,223–21,232, doi:10.1029/96JD01723.

Russell, J. I., M. G. Mlynczak, L. L. Gordley, J. Tansock, and R. Esplin (1999), Overview of the SABER experiment and preliminary calibration results, in *Proceedings of SPIE, 44th Annual Meeting, Denver, Colorado, July 18–23*, vol. 3756, p. 277.

Shiokawa, K., M. K. Ejiri, T. Ogawa, Y. Yamada, H. Fukunishi, K. Igarashi, and T. Nakamura (2003), A localized structure in OH airglow images near the mesopause region, *J. Geophys. Res.*, *108*(D2), 4048, doi:10.1029/2002JD002462.

Solomon, S. C., P. B. Hays, and V. J. Abreu (1984), Tomographic inversion of satellite photometry, *Applied optics*, *23*, 3409–3414.

Swenson, G., and C. Gardner (1998), Analytical models for the response of the mesospheric OH* and Na layers to atmospheric gravity waves, *J. Geophys. Res.*, *103*, 6271–6294, doi:10.1029/97JD02985.

Tarasick, D. W., and G. G. Shepherd (1992), Effects of gravity waves on complex airglow chemistries 2. OH emission, *J. Geophys. Res.*, *97*, 3195–3208, doi:10.1029/91JA02580.

Vargas, F., G. Swenson, A. Liu, and D. Gobbi (2007), O(^{1}S), OH, and O$_2$ (b) airglow layer perturbations due to AGWs and their implied effects on the atmosphere, *J. Geophys. Res.*, *112*, D14102, doi:10.1029/2006JD007642.

Walterscheid, R. L., G. Schubert, and J. M. Straus (1987), A dynamical-chemical model of wave-driven fluctuations in the OH nightglow, *J. Geophys. Res.*, *92*, 1241–1254.

Zhao, Y., M. J. Taylor, and X. Chu (2005), Comparison of simultaneous Na lidar and mesospheric nightglow temperature measurements and the effects of tides on the emission layer heights, *J. Geophys. Res.*, *110*, D09S07, doi:10.1029/2004JD005115.

Zwillinger, D. (1996), *CRC standard mathematical tables and formulae*, 30 ed., CRC Press.

———————————

F. Kamalabadi, A. Z. Liu, R. Nikoukar, and G. R. Swenson, Department of Electrical and Computer Engineering, University of Illinois at Urbana-Champaign, Coordinated Science Laboratory, Urbana, IL 61801, USA. (nikoukar@uiuc.edu)